Research Article

Johannes Stock*, Matthias Beier, Johannes Hartung, Sebastian Merx and Herbert Gross

Simulation and analysis of optical imaging systems including real freeform components

https://doi.org/10.1515/aot-2018-0065
Received December 4, 2018; accepted February 8, 2019; previously published online March 9, 2019

Abstract: In recent years, the precision of the manufacturing process for optical surfaces has improved tremendously. As a result, freefrom surfaces have become more attractive options for imaging applications with increased accuracy requirements. However, with regards the integration into an optical system, performance is often limited due to surface imperfections, such as mid-spatial frequency errors and alignment errors. This demonstrates the need for a more holistic description of systems, including multiple freeform components, which enable performance predictions based on the system as a whole. In this work, a solution for such a simulation is presented and verified by a comparison with the experimental data. This procedure not only predicts system performance but also supports tolerancing and easier alignment.

Keywords: freeform surfaces; optical design; optical fabrication.

1 Introduction

Technologies that are capable of manufacturing reflective or refractive optical surfaces without remaining symmetry are becoming increasingly available [1]. Non-rotational symmetric, high-performance systems can profit tremendously from the additional degrees of freedom offered by these optical freeform surfaces during the design process [2, 3]. For imaging applications, the manufacturing process typically involves diamond turning in combination with additional polishing methods [4, 5]. However, especially when dealing with shorter wavelengths, the requirements have increased for both the manufacturing and the optical design, along with the strongly correlated tolerancing for such systems. The limited precision of the turning process has resulted in surface deformations, such as more localized figure errors and characteristic, regular ripples within the mid-spatial frequency (MSF) range [6, 7]. This remains to be a limiting factor and should be considered when designing an optical system. Currently, there exist several comprehensive approaches for the analysis and simulation of different fabrication processes [8, 9], the theoretical description of surface imperfections on the point spread function (PSF) and the modulation transfer function (MTF) [10–13]. However, despite the introduction of these approaches, there remains a need for a more holistic simulation of even complex systems in order to close the gap between the optical design and the manufacturing. Our solution is based on an analytical description featuring a reasonable number of coefficients, thus allowing for the combined analysis and tolerancing of manufacturing deviations and alignment errors for multiple freeform components. In this paper, we present the verification of the approach for imaging systems. The description for real surfaces was introduced and discussed in our previous work [14]. For this purpose, the approach is applied in the current study to an anamorphic imaging telescope in the visible wavelength range [15], and the simulated wavefront – including the impact of real components – is compared to the measurements for the different fields.

The manuscript is structured as follows. In Section 2, the theory for describing real freeform surfaces is introduced. Section 3 discusses the integration of the manufactured components and the simulation of the system for an anamorphic imaging telescope. In Section 4, the results are analyzed and compared to the measured wavefronts from the assembled system. Afterwards, two examples are presented on how to tolerate the system based on this approach.

***Corresponding author: Johannes Stock,** Institute of Applied Physics, Friedrich-Schiller-Universität, Albert-Einstein-Str. 15, 07745 Jena, Germany, e-mail: johannes.stock@uni-jena.de
Matthias Beier and Johannes Hartung: Fraunhofer-Institut für Angewandte Optik und Feinmechanik IOF, Albert-Einstein-Str. 7, 07745 Jena, Germany
Sebastian Merx and Herbert Gross: Institute of Applied Physics, Friedrich-Schiller-Universität, Albert-Einstein-Str. 15, 07745 Jena, Germany

2 Theory

Our approach for the efficient integration into a simulated system of real optical surfaces, manufactured by diamond turning, is dependent on an analytical description based on a reasonable number of coefficients. This section briefly introduces the approach to make the following explanations more comprehensive, although more detailed analysis and discussion are provided within our previous work [14]. In general, the sag of the real surface z_{real} is decomposed into the ideal surface z_{ideal} and the deviations z_{dev}, which occur during manufacturing. Here, z_{real} is calculated using the equation

$$z_{\text{real}} = z_{\text{ideal}} + z_{\text{dev}}. \tag{1}$$

The ideal surface profile description, a result of the design process, typically comprises global polynomials, such as the Q- or Zernike-Polynomials [16, 17]. In comparison, the deviations are represented in our approach by the radial basis functions (RBFs) ϕ_{RBF}, which are used to describe the localized figure error z_{fig} and the additional MSF-functions z_{MSF} to also describe the regular, characteristic ripples resulting from the diamond-turning process. The calculations are performed using the equations below

$$z_{\text{dev}}(x, y) = z_{\text{fig}}(x, y) + z_{\text{MSF}}(r, \varphi), \tag{2}$$

$$z_{\text{fig}}(x, y) = \sum_n c_n \cdot \phi_{\text{RBF}}(x - x_n, y - y_n, \varepsilon_n), \tag{3}$$

$$z_{\text{MSF}}(r, \varphi) = \sum_n (a_n \sin(k_n r) + b_n \cos(k_n r)) \cdot \cos(m_n(\varphi + \varphi_0)) \cdot \gamma_n(r). \tag{4}$$

RBFs can, for example, be Gaussian-functions with a certain shape ε_n, laterally shifted on a grid (x_n, y_n). The height of each function c_n is determined by a least-square-approximation [18]. The MSF-functions in polar coordinates (r, φ) are a linear combination of radial symmetric rings, multiplied by an azimuthal dependent term with order m. An additional function $\gamma(r)$ is necessary to overcome the singularity at $r = 0$. In general, the center of the description does not need to be coincide with that of the surface aperture. The coefficients a_n, b_n and c_n are approximated by using least squares, and the spatial frequencies k_n are determined directly from the power spectral density function (PSD) of the corresponding surface measurements. This can be done in a one-dimensional or in an extended two-dimensional representation [19], where the azimuthal dependencies are also considered. In Figure 1, the resulting fit of an example surface based on the PSD is shown. The low spatial frequencies are covered by the RBFs, with this range being further extended by the additional MSF functions. The deviations seen are mostly caused by the unstructured deformations. The detailed results for the studied system are discussed within the next section.

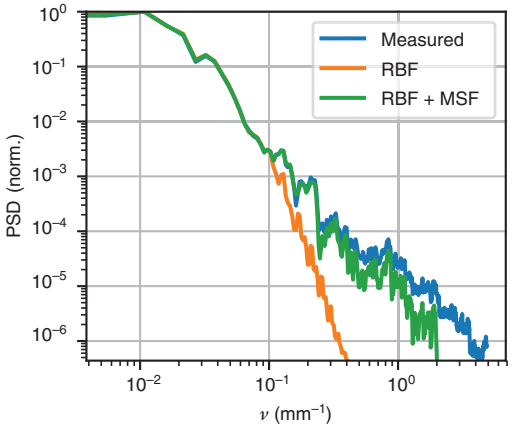

Figure 1: The normalized, one-dimensional power spectral density for the measured surface deformations (blue) of M1 (see Figure 2), the corresponding fit based on 250 RBFs (orange) and the fit with an additional 75 MSF-functions (green).

In summary, this approach allows for a description of real surfaces by using a reduced number of coefficients to make a re-import into the design, and simulation by ray tracing possible. For the typical surface deformations, figure error and regular MSF ripples are included within a remaining rms-deviation in the range of 1%–5% compared with the measurement. This corresponds to an rms-error in the range of a few nanometers for the examples in this contribution.

3 System integration and simulation

The integration of real surfaces into the performance simulation is demonstrated here using an afocal, anamorphic imaging telescope in the visible wavelength range as an example [15]. Such a system is typically used as front optics for spectrometers in space applications. Figure 2 illustrates the basic layout of this system. The goal of mapping a rectangular entrance pupil onto a square shaped exit pupil is achieved by using four freeform-shaped mirrors (M1 to M4). The individual surface of each

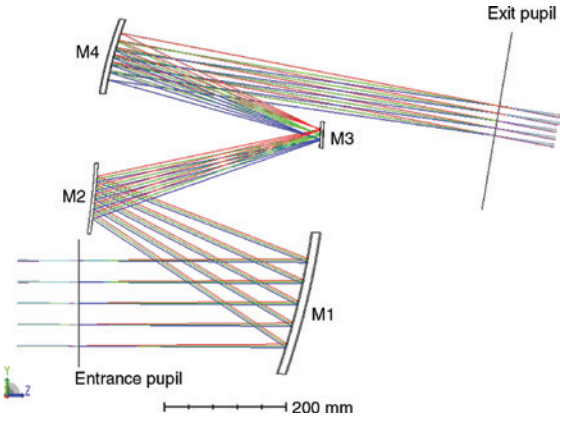

Figure 2: The layout of the optical design for the afocal, anamorphic imaging telescope. The rectangular entrance pupil is mapped on the square shaped exit pupil by four freeform mirrors (M1–M4).

mirror is a freeform [15], even if their ideal surfaces are described in the optical design by the off-axis, anamorphic aspheres. The system is designed for a ±3.22° field of view along the x-axis and ±0.47° along the y-axis. The mirrors are manufactured through a diamond turning process. To reduce the degrees of freedom involved in the assembly and alignment process, the mirrors M1 and M3, as well as mirrors M2 and M4, are manufactured on the same substrate.

To analyze the impact of deformations on the manufacturing process, the measured surfaces are fitted and reimplemented into the optical design. This is achieved through the analytical description explained within Section 2. In Figure 3, the measurements of the manufactured mirrors, captured by interferometry, are presented together with their corresponding analytical descriptions. The residual rms-error of the deviations between the measurement and fit is in the range of a few nanometers. These are mostly unstructured errors that are not captured by this approach, although they may still be included by statistical methods or as an additional optical path length error of the rays [20]. Notably, the quality of the description is strongly dependent on the measurement. For example, the bump in the center of M4 or the horizontal line on M1 are artifacts of their measurements, which are verified later when comparing the results with a measured wavefront.

The analytical expressions of the mirrors are implemented back into the optical design in the next step. This can be done, for example, in the Zemax OpticStudio [21], along with a dynamic link library (DLL). The limited number of surface profile coefficients allows for a fast simulation by ray tracing.

4 Results

The performance of the system can be evaluated by integrating the simulation with the real surface profiles. It is common to analyze the wavefront in the exit pupil as a criterion for the quality of high-performance systems. The presented approach can also be used to study the modulation transfer function (MTF) or the geometric spot diagrams.

Prior to including any manufacturing deformations, the wavefronts of the ideal designed surface shapes and their corresponding perfect component adjustments for the anamorphic telescope are shown in Figure 4. The wavelength is 632.8 nm. The results for the three exemplary fields are shown. The central field intersects the entrance pupil at 0°, and the angle of the two outer fields is ±0.235° along the *y*-axis. The rms-error of the wavefront for the central field is 43 nm with pv-error of 385 nm. For the two outer fields, the rms-errors are 43 and 44 nm for ±0.235° and −0.235°, respectively. The pv-errors differ slightly from the central field by 257 and 496 nm, respectively. Therefore, the system can be considered diffraction-limited for the specific wavelength.

The next step considers the real surfaces, as described in Section 3. The geometric spot diagrams of the central field for the ideal and the real systems are shown in Figure 5. The rms-radius is increased by a factor of 6 to 0.06 mrad. Figure 6 shows the simulated wavefronts for the exemplary fields in the upper row with the same wavelength of 632.8 nm. As expected, the performance of the system has decreased due to the impact of the manufacturing deformations on the mirrors. For example, the rms-error of the wavefront for the central field has increased by a factor of 6.5 to 281 nm. Both the impact of the figure error as well as the influence of the characteristic MSF-ripples from the turning process can be clearly investigated. Considering the deformation of the mirror M4 (see Figure 3), the 'blue bow' is almost directly mapped into the wavefront. This is because M4 is closest to the exit pupil. With increasing field angle, a shift of the structures coming from the more field correlated mirrors M1 and M4 is investigated.

As proposed in the beginning, the goal of this manuscript is to demonstrate the approach on an example system and its verification for tolerancing by a comparison with the experimental data. Quantitatively, the wavefronts in the exit pupil of the adjusted, afocal telescope were measured by interferometry in a double pass arrangement. The corresponding measurements are presented in the lower row of Figure 6. For all the studied field points,

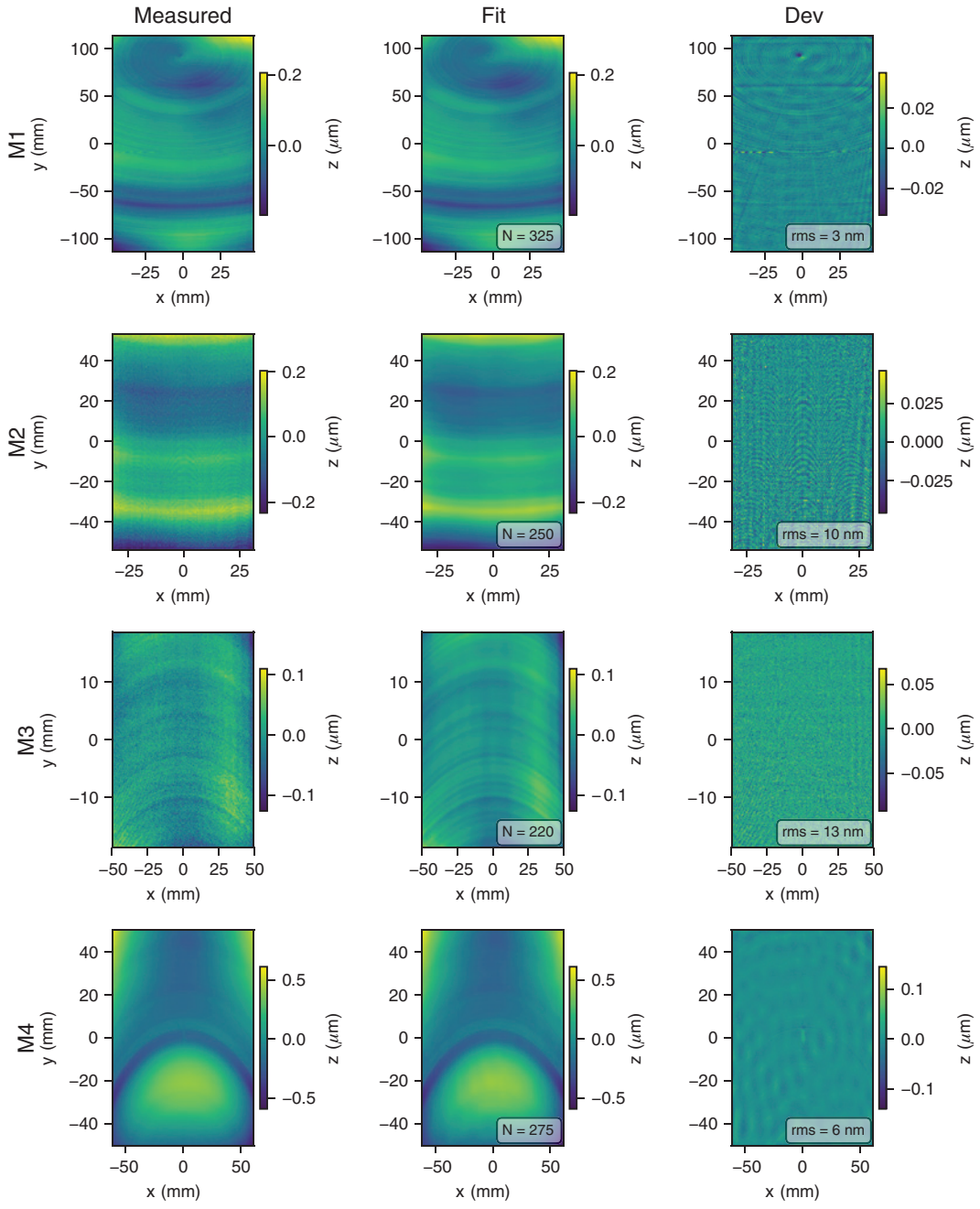

Figure 3: In the left column, the measured surface deformations for mirrors M1–M4 are shown. In the remaining columns, the corresponding fit and deviations to the measurements are presented. The rms-error and the total number of functions *N* are included in the figures (M1: 250 RBFs + 75 MSFs, M2: 200 RBFs + 50 MSFs, M3: 170 RBFs + 50 MSFs and M4: 200 RBFs + 75 MSFs). The scaling of the *x*- and *y*-axes is not equal.

good qualitative correlation is achieved. Both the figure error and the fine radial ripple structures of the measurement are resolved in the simulation. Quantitatively, the rms-error between the simulation and the corresponding measurements deviates by only 2.9% for the central field and by 2.6% and 3.0% for the outer fields, respectively. One reason for the low residual variation is the impact of the alignment process. A shift and a tilt between the two substrates was considered for the simulation to further improve the correlation with the measurements. The influence on the optical performance is shown in Figure 7. The residual degrees of freedom of the alignment procedure for assembling the experimental system influence its actual optical performance. In addition, the experimental

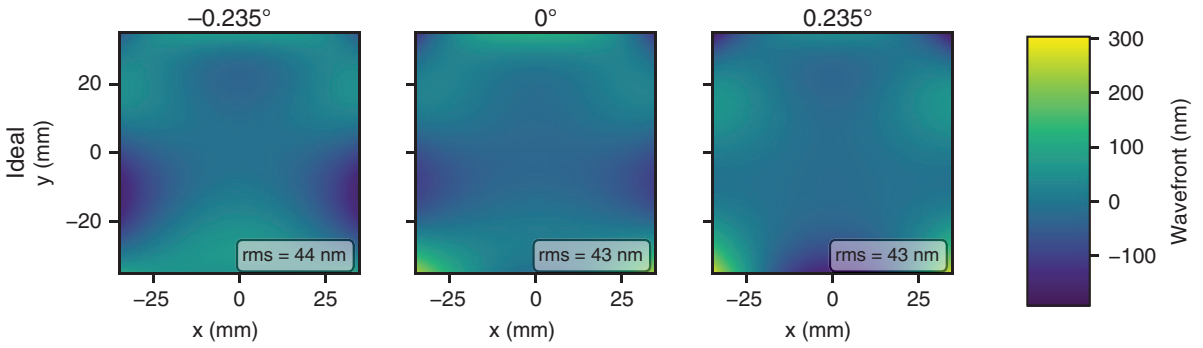

Figure 4: The simulated wavefronts based on the ideal optical system for an incoming field of –0.235°, 0° and 0.235° in the *y*-direction. The wavelength is $\lambda = 632.8$ nm. The rms-errors are 44 nm, 43 nm and 43 nm, respectively.

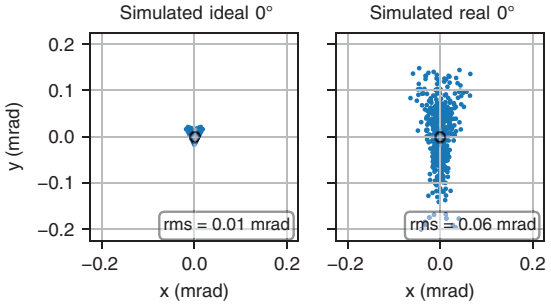

Figure 5: The geometric spot diagrams based on the ideal (left) and the manufactured optical surfaces (right) for the central field. The wavelength is $\lambda = 632.8$ nm. The rms-radii are 0.01 mrad and 0.06 mrad, respectively. The black circle represents the Airy-radius.

evaluation of the wavefront as well as the measurement and description of the mirrors are incorporated with a certain error, as discussed in Section 3.

Based on the analytical representation of the real surfaces, further analysis and tolerancing of the surface shape are possible by adjusting the corresponding coefficients. This can be done independently for both the figure error and the MSF-structures. The following provides two cases that are studied based on the imaging telescope. For the first example, the figure error of the mirrors M1 and M3, which are manufactured on the same substrate, is reduced by 50%. In Figure 8, the result of the simulation for the central field and a wavelength of 632.8 nm is

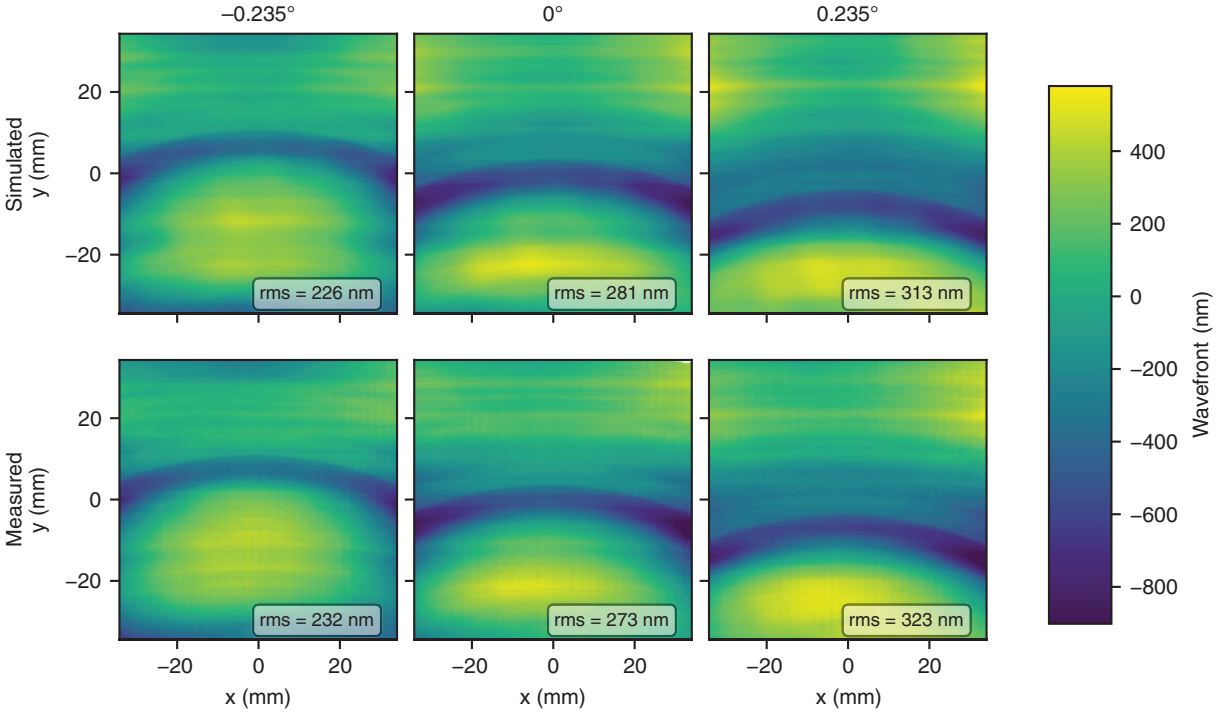

Figure 6: In the top row, the simulated wavefronts based on the real components are shown for a field of –0.235°, 0° and 0.235° along the *y*-axis. The wavelength is $\lambda = 632.8$ nm. The rms-errors are 226, 281 and 313 nm, respectively. In the bottom row, the corresponding measurements of the assembled system are presented for comparison. The rms-errors are 232, 273 and 323 nm, respectively.

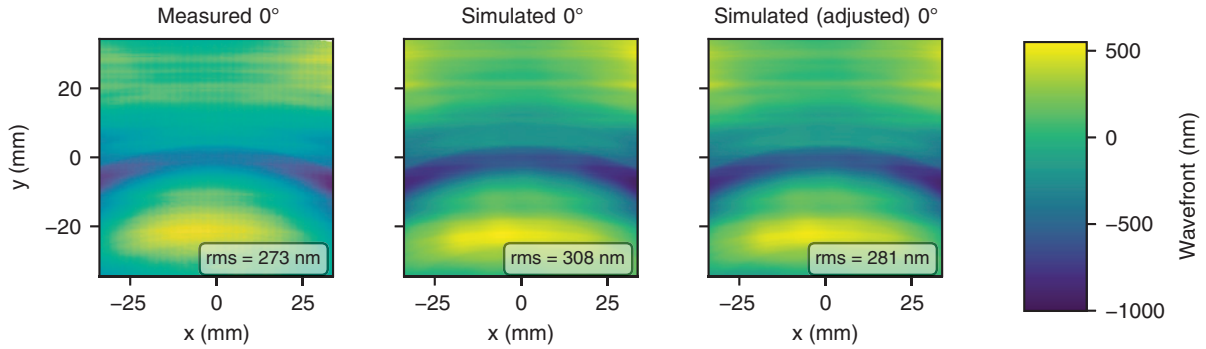

Figure 7: The measured and simulated wavefronts based on the real components are shown for the central field. In the figure to the right, an adjustment (tilt and shift) of the two substrates is incorporated. The wavelength is $\lambda = 632.8$ nm. The rms-errors are 273, 308 and 281 nm, respectively.

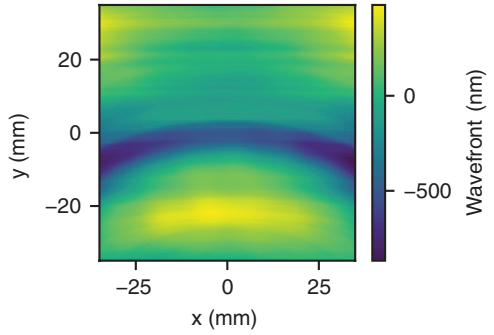

Figure 8: The simulated wavefront with a 50% reduced figure error of the mirrors M1 and M3, manufactured on the same substrate. The wavelength is $\lambda = 632.8$ nm and the rms-error is 261 nm.

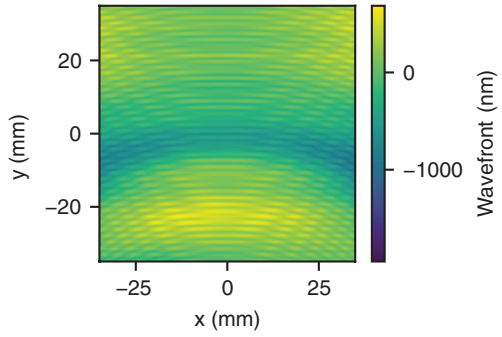

Figure 9: The simulated wavefront for the artificial MSF-structures ($a = 50$ nm, $\nu = 0.5$ mm^{-1}) on the mirrors M2 and M4, manufactured on the same substrate. The wavelength is $\lambda = 632.8$ nm and the rms-error is 296 nm.

shown. The rms-error is decreased only slightly to 261 nm due to the fact that the figure error of the last mirror, M4, is dominating. As expected, the regular ripple structures are not affected. The simulated wavefront in the same configuration but for tolerating the MSF-structures is presented in Figure 9. For this example, artificial surface ripples with a spatial frequency of $\nu = 0.5$ mm^{-1} and an amplitude of $a = 50$ nm were introduced on the second substrate with mirrors M2 and M4. The center is defined to be the same as that of the manufacturing process. It is important to consider that, due to the different positions of the surfaces relative to the pupils of the system and their different footprints, the sum- and difference-frequencies can arise in the wavefront [22]. The resulting rms-error for this example is 296 nm. In general, not only can the impact of the surface deformations be analyzed and tolerated based on this approach, but also the combined effects from the adjustment procedure, such as the tilts and shifts of the components.

5 Conclusion

In this contribution, our approach for the simulation of imaging systems, including the impact of real freeform components, was presented and demonstrated for an example system. The approach was verified with an rms-accuracy below 3% by comparing the simulation results against a measured wavefront of the assembled system. The usage of an analytic description to tolerate the shape of the optical surfaces was also demonstrated. The extension of the approach to high spatial frequency errors and the inclusion of even more mechanical degrees of freedom into the simulation is part of our ongoing research.

Acknowledgments: The authors would like to thank the Federal Ministry of Education and Research (BMBF) for funding this work, as part of the project Wk+fo+ (Funder Id: 10.13039/501100002347, 03WKCX1C). Parts of the research were supported by the German Aerospace Center (DLR) within the project VISTEL (Funder Id: 10.13039/501100002946, 50EE1224). Johannes Stock

would like to thank the Carl-Zeiss-Stiftung for supporting the research and Joshua Goncalves for several comments on the manuscript.

References

[1] F. Z. Fang, X. D. Zhang, A. Weckenmann, G. X. Zhang and C. Evans, CIRP Ann. 62, 823–846 (2013).
[2] B. Chen and A. M. Herkommer, Appl. Opt. 56, 901–906 (2017).
[3] C. Liu and H. Gross, Appl. Opt. 57, 5758–5768 (2018).
[4] J. Hartung, M. Beier and S. Risse, in 'SPIE Optical Systems Design', 10 (2018).
[5] G. Yu, H. Li and D. Walker, J. Eur. Opt. Soc. RP 6, 11044 (2011).
[6] G. W. Forbes, in 'SPIE Optical Measurement Systems for Industrial Inspection', 95251B (2015).
[7] M. Maksimovic, in 'SPIE Optical Systems Design', 14 (2015).
[8] M. Pohl and R. Börret, J. Eur. Opt. Soc. RP 11, 16010 (2016).
[9] O. Faehnle, M. Doetz, and O. Dambon, Adv. Opt. Technol. 6, 349–358 (2017).
[10] R. J. Noll, Opt. Eng. 18, 137–142 (1979).
[11] W. B. Wetherell, in 'SPIE Image Quality', 77–93 (1981).
[12] J. M. Tamkin, T. D. Milster and W. J. Dallas, Appl. Opt. 49, 4825–4835 (2010).
[13] J. M. Tamkin, W. J. Dallas and T. D. Milster, Appl. Opt. 49, 4814–4824 (2010).
[14] J. Stock, A. Broemel, J. Hartung, D. Ochse and H. Gross, Appl. Opt. 56, 391–396 (2017).
[15] M. Beier, J. Hartung, T. Peschel, C. Damm, A. Gebhardt, et al., Appl. Opt. 54, 3530–3542 (2015).
[16] G. W. Forbes, Opt. Exp. 20, 2483–2499 (2012).
[17] A. Broemel, U. Lippmann and H. Gross, Adv. Opt. Technol. 6, 327–336 (2017).
[18] G. E. Fasshauer, Meshfree Approximation Methods with MATLAB. World Scientific, (2007).
[19] T. Pertermann, J. Hartung, M. Beier, M. Trost, S. Schröder, et al., Appl. Opt. 57, 8692–8698 (2018).
[20] R. N. Youngworth and B. D. Stone, Appl. Opt. 39, 2198 (2000).
[21] Zemax, OpticStudio 18.7 User Manual. Zemax LLC, (2018).
[22] J. M. Tamkin and T. D. Milster, Appl. Opt. 49, 6522–6536 (2010).